Corrosion of Zirconium in the Context of the Spent Nuclear Fuel Reprocessing Plant

B. Gwinner, H. Badji-Bouyssou, M. Benoit, N. Brijou-Mokrani, P. Fauvet, N. Gruet, P. Laghoutaris, F. Miserque, R. Robin, M. Tabarant

HAL Id: cea-02491643
https://cea.hal.science/cea-02491643

Submitted on 26 Feb 2020

Corrosion of Zirconium in the Context of the Spent Nuclear Fuel Reprocessing Plant

B. Gwinner[a], H. Badji[b], M. Benoit[a], N. Brijou-Mokrani[a], P. Fauvet[c], N. Gruet[a], P. Laghoutaris[a], F. Miserque[d], R. Robin[a], M. Tabarant[b]

[a] CEA, DEN, DPC, SCCME, Laboratoire d'Etude de la Corrosion Non Aqueuse, F-91191 Gif-sur-Yvette, France.
[b] CEA, DEN, DPC, SEARS, Laboratoire d'Ingénierie des Surfaces et Lasers, F-91191 Gif-sur-Yvette, France.
[c] CEA, DEN, DPC, Service d'Etude de la Corrosion et du Comportement des Matériaux dans leur Environnement, F-91191 Gif-sur-Yvette, France.
[d] CEA, DEN, DPC, SCCME, Laboratoire d'Etude de la Corrosion Aqueuse, F-91191 Gif-sur-Yvette, France.
Tel: +33(0)169081640, Fax: +33(0)169081586, Email: benoit.gwinner@cea.fr

Abstract *–Zirconium is used as material for various applications in spent nuclear fuel reprocessing plants involving concentrated nitric acid medium under highly corrosive oxidizing conditions. In such conditions, zirconium can show two different oxidation regimes as a function of potential. At high potentials, the oxidation current is relatively important (few µA/cm^2) and constant with time. A poorly protective black oxide layer (ZrO$_2$) is formed on the surface, which has a thickness of few micrometers. At low potentials, the oxidation current decreases with time and progressively tends to low values (few nA/cm^2). This protective effect has been attributed to the formation/growth of a nanometric oxide layer (ZrO$_2$) on the surface. The thickness evolution of this layer has been simultaneously estimated as a function of time by in-situ electrochemical methods (Electrochemical Impedance Spectroscopy (EIS) and coulometry) and by ex-situ X-ray Photoelectron Spectroscopy analyses (XPS). These experimental results have been successfully compared with an anodic oxide layer growth model based on the high field regime.*
The addition of small amounts of fluorine in nitric acid (a few tenths of millimoles per liter) modifies notably the corrosion processes. Three phases are observed in the corrosion mechanism: (1) a first incubation phase where the corrosion rate is negligible, (2) a second phase with a sharp increase of the corrosion rate (the SEM observations show a process of nucleation / growth / coalescence of pits) and (3) a third phase with a progressive decrease of the corrosion rate (corresponding to a generalized corrosion mechanism by an oxidation/complexation process limited by the supply of the reactive species).

I. INTRODUCTION

In France, the spent nuclear fuel reprocessing is based on the PUREX chemical process (Plutonium and Uranium Refining by EXtraction). The preliminary steps are: shearing of fuel clads; dissolution of spent fuel in nitric acid; recovery of insoluble solids by clarification. Then the PUREX process is used to: extract uranium and plutonium by an organic solvent (tributylphosphate); recover fission products in nitric acid phase; extract plutonium from the uranium/plutonium solution by reduction of plutonium; purify, concentrate and chemically transform uranium and plutonium. The products are plutonium which can be used with depleted uranium for MOX fuel manufacturing, and uranium enriched at the level of the spent fuel.

As a consequence of the use of nitric acid to dissolve oxide spent fuel, various nitric media are found throughout the process. Nitric acid is at concentrations almost up to the azeotropic level (14.4 mol/L) and at temperatures up to slightly higher than their boiling -temperature (120 °C for 14.4 mol/L HNO$_3$). These nitric media may be more or less renewed, depending on the equipment (*e.g.* fuel dissolver, fission products concentrators, acid recovery evaporators, fission products storage tanks).

In order to properly contain these strongly acidic and oxidizing media, metallic materials have been chosen according to their corrosion limits, optimized and qualified before the building of the plants[1,2]. These materials are mainly:

- very low carbon austenitic stainless steels (type AISI 304L, 316L and 310L) for the major part of the equipments[3,4,5,6];
- a special stainless steel with 4 wt. % silicon, for the fission product evaporators[7];

- and zirconium, chosen for the construction of most critical equipments in term of corrosion, such as fuel dissolvers and nitric acid recovery concentrators[8,9,10,11]. Indeed in some cases (in strong oxidizing media), stainless steels can show limits with high corrosion rates and, for some of them (AISI 304L, 316L and 310L), with intergranular corrosion[12,13,14].

It is known that zirconium has a high corrosion resistance in such oxidizing media like nitric acid. But zirconium has also a high sensibility to the presence of fluorine in nitric acid[1,2]. The aim of this paper is to give new insights on the corrosion processes of zirconium in nitric acid in absence (§ III) and in presence (§ IV) of small amounts of fluorine.

II. EXPERIMENTAL SET-UP

All experiments were performed in a 500 mL cell in a 3-electrodes configuration. The working electrode was a rotating ring disk electrode of zirconium (surface area = $0.5 - 1$ cm^2) so as to control the hydrodynamics on the surface. The counter-electrode was a platinum basket. The reference electrode was a Mercury Sulfate Electrode (Hg-Hg$_2$SO$_4$ - MSE, E = 0.658 V/NHE) protected from the electrolyte with a salt bridge. All the potentials in the paper are given vs. NHE. The potentiostat used for all the experiments was a Biologic VSP.

The zirconium was Zr 702 grade, which composition is given in Table I[15].

TABLE I

ASTM analytical specifications of zirconium 702 (wt.%)

(Zr+Hf)$_{min}$	Hf$_{max}$	(Fe+Cr)$_{max}$	H$_{max}$	N$_{max}$	C$_{max}$	O$_{max}$
99.2	4.5	0.2	0.005	0.025	0.05	0.16

The corrosion behavior of zirconium was studied in HNO$_3$ 6 mol/l at 30 °C. The nitric acid solutions were prepared by diluting R.P. NORMAPUR PROLABO 52.5 % solutions with demineralized water. In some cases fluorides were added from NaF salts.

Different electrochemical experiments were performed: Linear Voltammetry (LV), ChronoAmperometry (CA) and Open Circuit Potential (OCP).

The concentration of zirconium dissolved in solution was periodically determined using Inductively Coupled Plasma Atomic Emission Spectroscopy (ICP-AES – Optima 2000 model from Perkin-Elmer).

The surface of the samples was *ex-situ* observed with an inversed optical microscope (Olympus GX51) or with a scanning electron microscope (SEM Leo 1450 VP Zeiss or Ultra 55 Zeiss).

The chemical composition of the zirconium surface was also *ex-situ* analyzed with X-Ray Photoelectron Spectroscopy (XPS). The samples were irradiated with a X ray beam (monochromatic aluminium K-alpha with photons energy of 1,486.6 eV). The kinetic energy of escaping photoelectrons was simultaneously measured with a spectrometer (Thermofisher Escalab 250 xi). The spot diameter was 900 μm.

III. CORROSION OF ZIRCONIUM IN PURE HNO$_3$

III.A. Thermodynamic considerations

Some preliminary considerations are given in this paragraph on the reactions occurring in the corrosion of zirconium by nitric acid.

As illustrated by the potential-pH diagram[16] for the nitrogen-water system (Fig. 1), nitric acid has mainly two properties that are important for corrosion. On the one hand, protons give acid properties. It has to be mentioned that nitric acid is not a strong acid at high concentrations. On the other hand, nitrates give oxidizing properties. The nitrates reduction is a complex reaction producing reduced species like HNO$_2$, NO$_2$, NO or N$_2$O which can be under liquid or gaseous form. These reactions are also complex on a kinetic point of view with autocatalytic processes[17,18,19,20]. In a first approximation, it is supposed that the reduction current is mainly due to the reduction of acid nitric into nitrous acid according to:
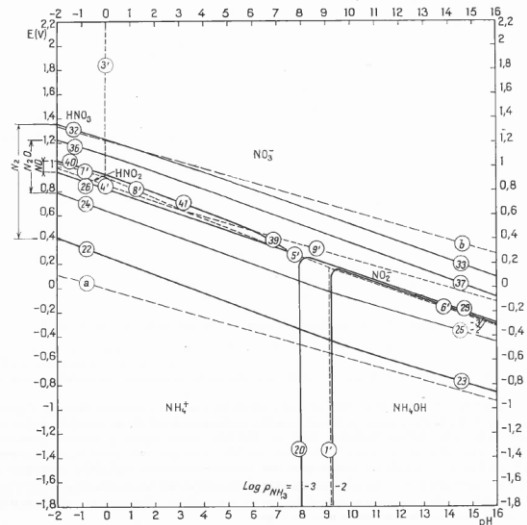
$$HNO_3 + 2e^- + 2H^+ \rightleftharpoons HNO_2 + H_2O \qquad (1)$$

Fig. 1. Potential-pH diagram[16] of the nitrogen-water system at 25 °C

The Fig. 2 illlustrates the oxido-reduction properties of zirconium. In contact with concentrated nitric acid (Fig. 1), this potential-pH diagram predicts that zirconium will be oxidized according to:

$$Zr \rightleftharpoons Zr^{4+} + 4e^- \qquad (2)$$

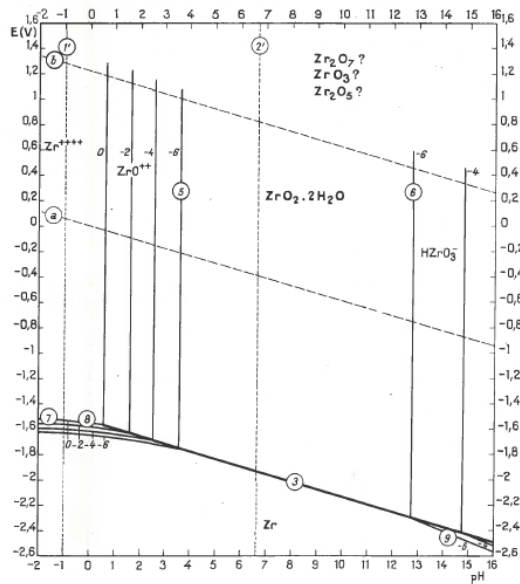The objective of the further paragraphs is to study the kinetics of this reaction.

Fig. 2. Potential-pH diagram[16] of the zirconium-water system at 25 °C

III.B. Oxidation kinetics

The oxidation behavior of zirconium was first studied with linear voltammetry experiments. The variation of the oxidation current density is reported in Fig. 3 as a function of the applied potential from the corrosion potential (1.1 V/NHE) to 5 V/NHE. Two domains can be distinguished. Up to around 3 V/NHE, the current density presents a low value (few tenths of $\mu A/cm^2$) and is independent of the potential. In this potential range, a non-uniform darkening of the surface is observed. Above 3 V/NHE an increase of the current density is observed as a function of potential. The surface becomes uniformly black. This is attributed to the formation of an oxide layer on the surface with a thickness of some tens of micrometers (Fig. 4).

With this dynamic method, a passive behavior is thus observed up to 3 V/NHE. In spite of the very low potential scan rate (0.04 mV/s) it is questionable if this is representative of a long term behavior of zirconium. Indeed the transition potential could be over-estimated if zirconium evolves slowly compared to the potential scan rate.
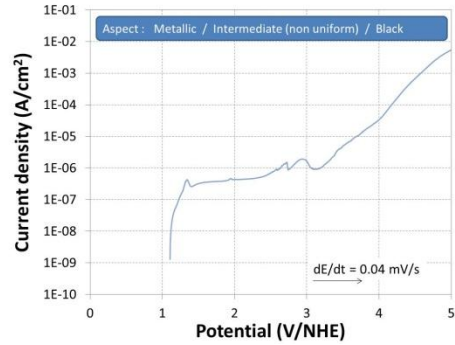

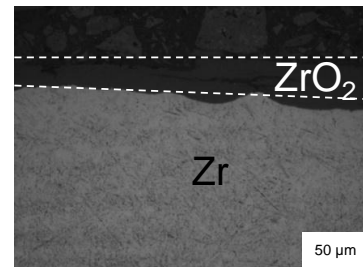Fig. 3. Linear voltammetry of zirconium in nitric acid 6 mol/l at 30 °C (dE/dt = 0.04 mV/NHE)

Fig. 4. Cross section of zirconium after the linear voltammetry in nitric acid 6 mol/l at 30 °C (dE/dt = 0.04 mV/NHE)

For that purpose chronoamperometry experiments were performed at different potential in the range 1.4 to 2.8 V/NHE. The results obtained at 1.4, 1.92 and 2.8 V/NHE are shown in Fig. 5. The oxidation current is given as a function of time (logarithmic scale). Two kinds of behaviors are observed depending of the potential.

For potentials lower than 1.85 V/NHE the current density decreases continuously. The oxidation current is attributed to the formation of the oxide layer. The thickness of this layer can then be estimated to some nanometers (see § III.C). The decrease of current density as a function of time illustrates the self-protecting effect of this oxide layer: the more the oxide layer thickness increases, the lower becomes the current density.

For potentials higher than 1.85 V/NHE the current density becomes unstable and does not decrease as a function a time. The oxide layer formed on the surface is in this case some micrometers thick (Fig. 4). The unstable current density can be connected with the non-dense aspect of the oxide layer. Indeed some cracks are observed in the oxide.
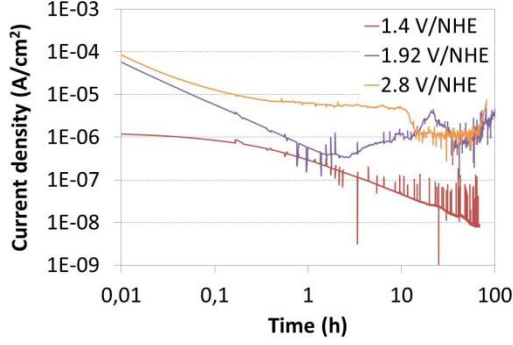
Fig. 5. Chronoamperometry at different potential of zirconium in nitric acid 6 mol/l at 30 °C (X axes expressed in logarithmic scale)

All the previous results are summed up in Fig. 6. For potentials lower than 1.85 V/NHE zirconium is strictly passive: a protective oxide layer (some nanometers thick) is formed (see § III.C). As a consequence the oxidation current density decreased continuously to negligible values. For potentials higher than 1.85 V/NHE zirconium is not strictly in its passive stable: an oxide layer (some micrometers thick) is formed which contains cracks. As a consequence the current density is quite constant and the oxide grows continuously at a constant rate.
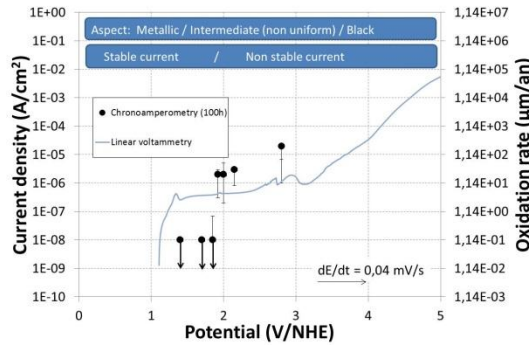

Fig. 6. Synthesis of the results (LV, CA) concerning the oxidation kinetics of zirconium in nitric acid 6 mol/l at 30 °C

In the following paragraphs we will focus in characterizing the system in its passive state.

III.C. Passive layer thickness measurements

The oxide layer formed in the passive domain during CA measurements was characterized by three different ways.

Ex-situ X-ray Photoelectron Spectroscopy (XPS) measurements were periodically carried out on the surface. An example of spectrum focused the *Zr-3d* core levels is given in Fig. 7. Two contributions can be observed: an oxide contribution (Zr-$3d_{5/2}$ = 183.2 eV and Zr-$3d_{3/2}$ = 185.6 eV) and a metallic contribution (Zr-$3d_{5/2}$ = 179.2 eV and Zr-$3d_{3/2}$ = 181.6 eV). Supposing that XPS response is due to a continuous oxide layer over the underlying metallic substrate, the oxide thickness can be estimated according to Eq. 3[22].

$$ d = \lambda_{ox} \cos\theta \, ln\left[\frac{N_{met}}{N_{ox}} \times \frac{\lambda_{met}}{\lambda_{ox}} \times \frac{I_{ox}}{I_{met}} + 1\right] \qquad (3) $$

With:

- I_{met} and I_{ox}, the intensity of *Zr-3d* core levels under metallic and oxide form;
- λ_{met} et λ_{ox}, the inelastic mean free paths of *Zr-3d* photoelectrons in metal and oxide. These parameters were estimated according the semi-empirical Seah & Dench approach[23];
- N_{met} and N_{ox}, the concentration of atoms per volume unit;
- θ, the angle between the detector and the normal to the sample (in these measurements, $\theta = 0°$).
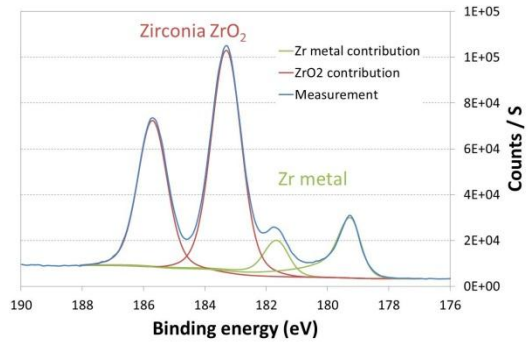

Fig. 7. Example of XPS Zr-*3d* spectrum

The second method to estimate the oxide layer thickness was the coulometric balance from the oxidation current. Supposing that all the charge is used to elaborate the oxide layer (hypothesis supported by the fact that all the ICP-AES measurements of zirconium in solution are under the detection limit of 8 ng/mL) the Faraday's law[21] is used to estimate the oxide layer thickness increase *Δd* from the total oxidation charge *Δq* (Eq. 4):

$$ \Delta d = \frac{\Delta q M}{nF\rho_{ox}} \qquad (4) $$

The third method was to perform electrochemical impedance spectroscopy (EIS) periodically during CA measurements. An example of EIS spectrum is given in Fig. 8 (Bode diagram). In a first approximation, only a constant time is observed. The capacitive behavior can be attributed to the oxide layer which by its dielectric properties plays the role of condenser. Moreover it is observed that the slope of the modulus as a function of the logarithms of frequency is not strictly equal to -1 (values comprised between 0.9 and 0.95) and the minimum of the phase is not strictly equal to 90°. As a consequence the system does not behave as a pure capacitance. It is proposed to model this non-ideal behavior with the power law model which had previously succeeded in modeling similar systems[24]. This model associates this non-ideal behavior to the distribution of resistivity along the oxide layer thickness. It is shown that this distribution of

resistivity globally behaves electrochemically as a Constant Phase Element (CPE). With the CPE parameters (Q and α, determined by adjustment on experimental spectra) the oxide layer thickness can be estimated according to Eq. 5.

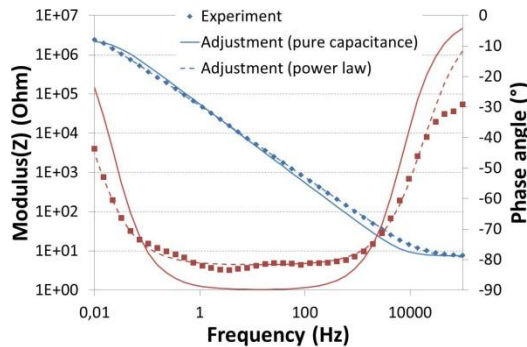$$d = \frac{(\varepsilon\varepsilon_0)^\alpha}{gQ\rho_d^{1-\alpha}} \quad (5)$$

Fig. 8. Example of EIS spectrum

These three methods were used during three CA measurements made in the same conditions (HNO$_3$ 6 mol/l at 30 °C, 1.4 V/NHE) to test the reproducibility, but stopped at different times (1, 20 and 100 h). The results are given in Fig. 9. In a first approximation, the evolution of the oxide layer thickness results is consistent for the three CA experiments and for the three methods used to estimate the oxide thickness (XPS, coulometry and EIS). Nevertheless the XPS seems to give a larger value than those estimated by coulometry or EIS. This can be possibly explained by the method for the evaluation of inelastic mean free paths of photoelectrons. This point is presently under investigation[25,26, 27].
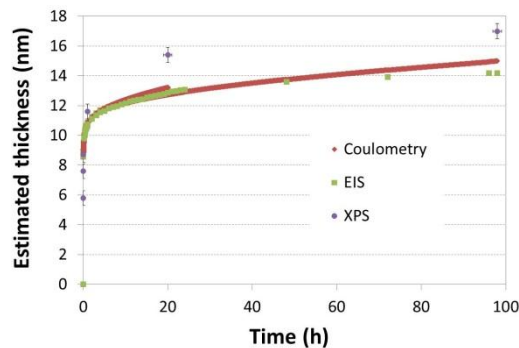

Fig. 9. Evolution of zirconium oxide thickness estimated by coulometry, EIS and XPS as a function of time (zirconium polarized at 1.4 V/NHE in HNO$_3$ 6 mol/l at 30 °C).

III.D. Passive layer growth and modeling

The aim of this paragraph is to try to adjust a physical law on the experimental results. A review has recently been published by MacDonald on the oxide growth models[28]. Concerning the model with no dissolution term (no

zirconium was measured in solution by ICP-AES), two families of models were distinguished.

For the "Place Exchange Model", "Interfacial Model" or "Point Defect Model" the oxide growth can be described according to Eq. 6:

$$\frac{dd}{dt} = a''e^{-b''d} \quad (6)$$

It can be shown (Faraday's law[21]) that the oxide growth rate dd/dt is directly proportional to the measured oxidation current. Thus in Fig. 10, it is traced the logarithms of the current density as a function of $-d$ for tree different CA experiments (HNO$_3$ 6 mol/l at 30 °C) in the passive domain (1.4, 1.7 and 1.85 V/NHE). In Fig. 10, a linear region is only observed after duration between 10 to 30 minutes (depending on the applied potential).
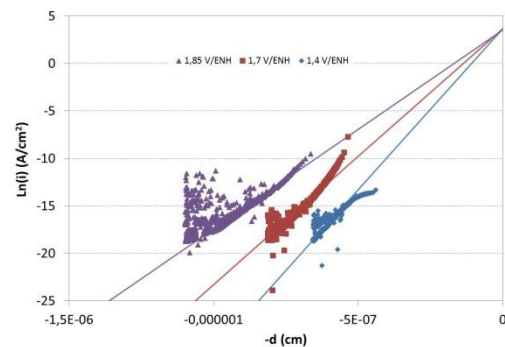

Fig. 10. Fitting of the "Point Defect Model" on experimental results (CA of zirconium at 1.4, 1.7 and 1.85 V/NHE, respectively in HNO$_3$ 6 mol/l at 30 °C)

For the "High Field Model" (well described by Lohrengel[29]), the oxide growth is modeled according to Eq. 7:

$$\frac{dd}{dt} = a'e^{b'/d} \quad (7)$$

To verify this law, the logarithms of the current density is traced in Fig. 11 as a function of $1/d$ for same CA experiments as in Fig. 10. A better consistency is observed in Fig. 11 than in Fig. 10, especially for the applied potentials 1.7 and 1.85 V/NHE. Nevertheless, the "High Field Model" seems to be not consistent at early time of the experiment at the potential 1.4 V/NHE. Similar cases have previously been explained by the state of the initial thickness present on the surface before CA experiment[29].
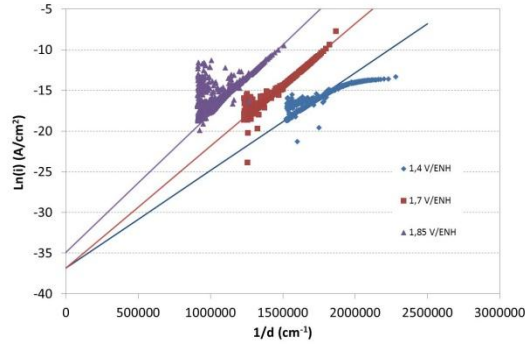
Fig. 11. Fitting of the "High Field Model" on experimental results (CA of zirconium at 1.4, 1.7 and 1.85 V/NHE, respectively in HNO$_3$ 6 mol/l at 30 °C)

As a conclusion the oxide growth experimentally observed seems to be better described by the "High Field Model". As an example, the adjustment of the "High Field Model" parameters on experimental data given in Fig. 9, is illustrated in Fig. 12.
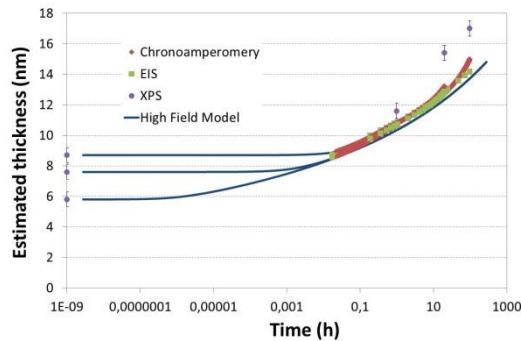

Fig. 12. Fitting of the High Field Model on experimental results (CA of zirconium at 1.4 V/NHE, respectively in HNO$_3$ 6 mol/l at 30 °C)

IV. CORROSION OF ZIRCONIUM IN HNO$_3$ WITH LOW FLUORINE CONTENT

The aim of this part IV is to study how the corrosion processes observed in pure nitric acid (§ III) are modified by the presence of small amounts of fluorine. Indeed the corrosion rate of zirconium is highly increased by the presence of fluorine[30]. But the exact corrosion mechanism seems still to be controversial[31-51]. The aim of this part is to give new insights on these aspects.

IV.A. Thermodynamic considerations

Some preliminary considerations are given in this paragraph on the speciation of fluorine in nitric acid solutions. Fluorine is introduced in nitric acid as NaF salt (§ II). As illustrated by the potential-pH diagram[16] for the fluorine-water system (Fig. 13), introduced fluorides (F$^-$) transform mostly into hydrofluoric acid (HF) in acid solutions like nitric acid.
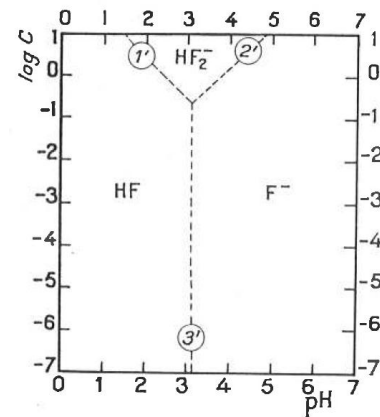

Fig. 13. Potential-pH diagram[16] of the fluorine-water system at 25 °C

IV.B. Corrosion kinetics in presence of fluorine

The zirconium electrode was first prepared by polarizing it during 1 h at 1.4 V/NHE in nitric acid 6 mol/l (without fluorine) at 30 °C. By this way an oxide layer with a controlled thickness (11-12 nm, § III) was obtained.

Then the electrode was put at open potential and fluorine (5.4 mg/l) was added. The corrosion kinetics was measured by two methods: zirconium released in solution analyzed by ICP-AES (dissolution kinetics) and the polarization resistance measured electrochemically (oxidation kinetics). The evolution of the corrosion rate (estimated from ICP-AES measurements) and the inverse of the polarization resistance is given in Fig. 14 as a function of time. Both kinetics are in accordance.
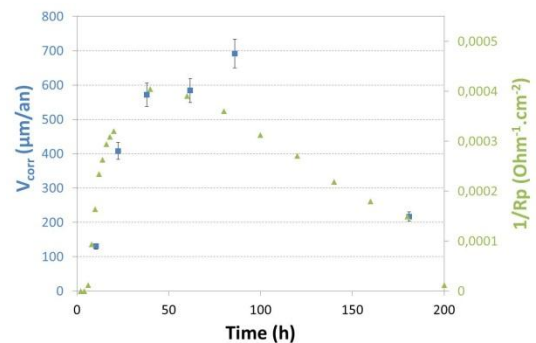

Fig. 14. Corrosion kinetics of zirconium in HNO$_3$ 6 mol/L, F 5,4 mg/L, 30 °C, 500 rpm, open circuit potential (initial oxide thickness: 11-12 nm)

The evolution of the surface morphology is given in Fig. 15 as a function of time.
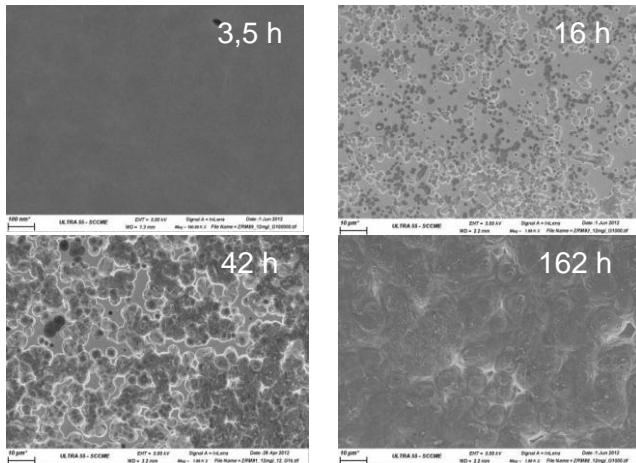
Fig. 15. SEM observations of zirconium corroded in HNO_3 6 mol/L, F 5,4 mg/L, 30 °C, 500 rpm, open circuit potential (initial oxide thickness: 11-12 nm)

In Fig 14, three phases are observed. From 0 to 4 hours, no dissolution of zirconium is measured. This is in accordance with Fig. 15, where no corrosion is observed. This first phase is called incubation phase and will be more precisely discussed in § IV.C.

From 4 to 50 h, dissolution of zirconium is observed and the rate increases as a function of time. This has to be associated to the apparition of pits at surface that first nucleate, grow and progressively coalesce. This point will be more precisely discussed in § IV.C.

From 50 h, the dissolution rate decreases progressively. The Fig. 15 shows that the corrosion is now generalized on the whole surface. The fact that the dissolution rate decreases as a function of time is discussed in § IV.D.

IV.C. Phases 1 and 2

The corrosion morphology shown after 16 h in Fig. 16 is observed at higher magnification to identify the processes occurring in a pit. Fig. 16 shows that the pit is partially covered by a layer that we attribute to the oxide layer. Moreover in the part which is not covered by this layer, the presence of "second" film is observed at the bottom of the pit. This "second" film appears to be complementary to the first one as illustrated by the dotted line in Fig. 16. From these observations, it is deduced that the oxide film is always present of the surface after 16 h corrosion but is partially broken on the pit. As consequence, it seems that the zirconium oxide is less soluble that zirconium itself.
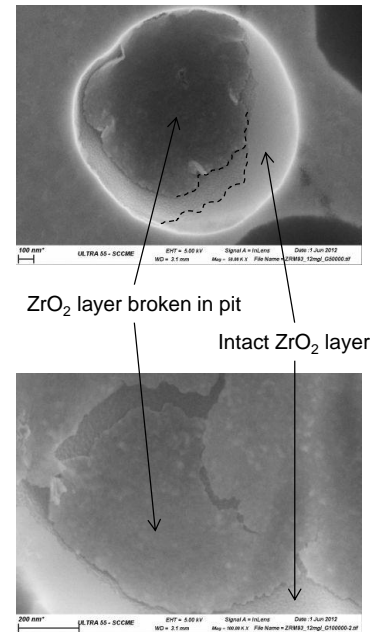

Fig. 16. SEM observations of zirconium corroded 16h in HNO_3 6 mol/L, F 5,4 mg/L, 30 °C, 500 rpm, open circuit potential (initial oxide thickness: 11-12 nm)

To confirm this result, similar experimentations were performed with different initial oxide layer thicknesses: 6-9 (native oxide), 30-40 nm (polarized 100 h at 1.4 V.NHE in HNO_3 6 mol/l at 30 °C), 800-1000 nm (oxidized under air at 550 °C during 6 h) and bulk (yttria stabilized) zirconia. For the four samples, the total zirconium dissolved in nitric acid 6 mol/l + fluorine 5.4 mg/l at 30 °C is given in Fig. 17 as a function of time. As previously suspected, it is observed that the bulk zirconia is not dissolved in these conditions. As a consequence, the zirconia layer could be viewed as a barrier towards corrosion by fluorine in nitric acid. This could explain the incubation time observed at the beginning of the corrosion kinetics. In Fig. 17, this incubation time seems to be directly proportional to the oxide layer thickness (duration experiment is probably too short to observe the corrosion zirconium with the 800-1000 nm zirconia layer).

These observations suggest two hypotheses. First, the incubation time could be explained by the slow dissolution of the oxide layer. When sufficiently thin, the oxide layer can allow the apparition of pits. Second, fluorine could diffuse through the oxide as suggested for titanium[52,53], accumulate and react at the zirconium/oxide interface, initiating pits. When the pit is sufficiently large, the oxide present over it breaks mechanically. This second hypothesis is further discussed in § IV.D.
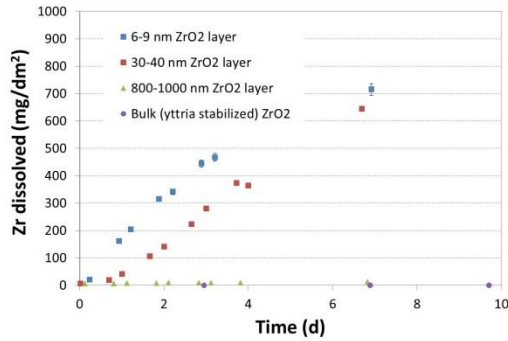
Fig. 17. Corrosion kinetics of zirconium in HNO_3 6 mol/L, F 5,4 mg/L, 30 °C, 500 rpm, open circuit potential (with different initial oxide thicknesses)

IV.D. Phase 3

When the pits coalesce, the corrosion affects the whole surface and becomes generalized. As previously discussed, the exact reaction at the interface is today controversial. In order to give a new insight on this point, XPS depth profiles were carried out on samples corroded in phase 3. The relative atomic concentration variation of zirconium, oxygen and fluorine is given in Fig. 18 as a function of erosion time. It is observed that at the extreme surface, the main elements are oxygen and zirconium (the binding energies – spectra not shown here – of Zr-*3d* core levels are coherent with the presence of ZrO_2). For intermediate erosion time, the main elements become fluorine and zirconium (the binding energies – spectra not shown here – of Zr-*3d$_{3/2}$* = 188.2 eV and Zr-*3d$_{5/2}$* = 185.8 eV pics seem to be coherent with ZrF_4[54-56]). For longer erosion time, the XPS spectra (not shown here) become characteristic of zirconium under metallic state.

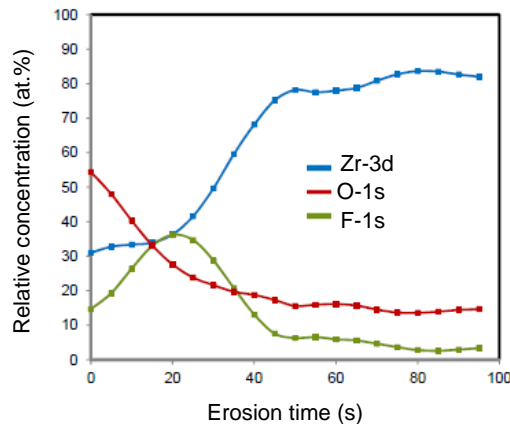These observations suggest that fluorine accumulates at the metal / oxide interface as previously proposed in § IV.C.

Fig. 18. XPS profile of zirconium corroded 140 h in HNO_3 6 mol/L, F 7.2 mg/L, 30 °C, 500 rpm, open circuit potential (initial ZrO_2 layer thickness 11-12 nm)

Moreover a 1D model (not detailed here) was developed (COMSOL) to simulate the evolution of the corrosion in phase 3. The main hypotheses are the following: the transport of the reactive specie (fluorine) is limited by diffusion, the reaction of fluorine at the zirconium surface is fast, corrosion products are ZrF_n^{4-n} complexes[33,57]. First calculations (not shown here) succeeded in reproducing the aspect of corrosion kinetics observed experimentally. Moreover they show that the corrosion process is limited by the supply of the reactive specie (flurorine).

V. CONCLUSIONS

It has been shown that in nitric acid, zirconium can have two different oxidation regimes as a function of potential. At high potentials, the oxidation current is relatively important (few $\mu A/cm^2$) and constant with time. An oxide layer (ZrO_2) is formed on the surface, which has a thickness of few micrometers and is poorly protective. At low potentials, the oxidation current decreases with time and progressively tends to low values (on the order of some nA/cm^2). This protective effect has been attributed to the formation/growth of a nanometric oxide layer (ZrO_2) on the surface. The thickness evolution of this layer has been simultaneously estimated as a function of time by electrochemical impedance spectroscopy (EIS) and coulometric in situ methods and by X-ray photoelectrons spectroscopy ex situ analyses (XPS). These experimental results (which are consistent from each other) have been successfully compared with an anodic oxide layer growth model based on the high field regime.

The addition of small amounts of fluorine in nitric acid (a few tenths of millimoles per liter) modifies notably the corrosion processes. Three phases are observed in the corrosion mechanism: an incubation phase where the corrosion rate is negligible, a second phase with a sharp increase of the corrosion rate (the SEM observations show a process of nucleation / growth / coalescence of pits) and a last phase with a progressive decrease of the corrosion rate (corresponding to a generalized corrosion mechanism by an oxidation/complexation process limited by the supply of the reactive species.

ACKNOWLEDGMENTS

REFERENCES

1. P. Fauvet, *Nuclear corrosion science and engineering*, p. 679-728, Woodhead Publishing (2012).

2. P. Fauvet et al., "Corrosion mechanisms of austenitic stainless steels in nitric media used in reprocessing plants", *Journal of Nuclear Materials*, **375**, *1*, p. 52 (2008).

3. J. Decours, J.C. Decugis, R. Demay, M. Pelras, G. Turluer, "Austenitic stainless steels – assessment of progress in materials performance for reprocessing applications", *Technical Committee Meeting on Materials Reliability in the Back-end of the Nuclear Fuel Cycle*, Vienna, Austria (September 2–5, 1986).

4. G. Pinard-Legry, M. Pelras, G. Turluer, "Corrosion resistance of metallic materials for use in nuclear fuel reprocessing. A Working Party Report on Corrosion in the Nuclear Industry", *EFC Publications 1*, The Institute of Metals (1989).

5. M. Leduc, M. Pelras, J. Sannier, G. Turluer, R. Demay, "Etudes de corrosion sur les matériaux destinés aux usines de retraitement", *Recod 87*, Paris (1987).

6. G. Pinard-Legry, M. Pelras, G. Turluer, "Corrosion resistance of metallic materials for use in nuclear fuel reprocessing", *Eurocorr 87*, Karlsruhe, Germany (April 6–10, 1987).

7. R. Robin, V. Spagnol, F. Miserque, "Correlation between composition of passive layer and corrosion behavior of high Si-containing austenitic stainless steels in nitric acid", *Journal of Nuclear Materials*, **375**, p. 65–71 (2008).

8. H. Chauve, R. Demay, J. Decours, M. Pelras, J. Simonnet, "Construction materials for spent fuel reprocessing plants", *Nuclear Europe*, **2**, p. 19-21 (1986).

9. H. Chauve, J. Decours, R. Demay, M. Pelras, J. Simonnet, G. Turluer, "Zirconium use for large process components", *Technical Committee Meeting on Materials Reliability in the Back-end of the Nuclear Fuel Cycle*, Vienna, Austria (September 2–5, 1986).

10. M. Leduc, A. Le Duigou, M. Pelras, "The use of zirconium in nitric environment – corrosion studies", *4th Symposium on Ti and Zr Industrial Applications (ASTM B.10)*, Philadelphia, Pa (October 10–11, 1984).

11. P. Fauvet, G. Pinard-Legry, "Corrosion aspects in reprocessing technology", *Eurocorr 92*, Espoo, Finland (May 31–June 4, 1992).

12. Q.T. Tran, V. Bague, "A method to determine the intergranular corrosion rate of stainless steel in concentrated nitric acid", *Eurocorr 2006*, Maastricht, the Netherlands (September 25–28, 2006).

13. V. Bague, S. Chachoua, Q.T. Tran, P. Fauvet, "Determination of the long-term intergranular corrosion rate of stainless steel in concentrated nitric acid", *Journal of Nuclear Materials*, **392**, p. 396–404 (2009).

14. B. Gwinner et al., "Corrosion intergranulaire dans l'acide nitrique des aciers inoxydables austénitiques non sensibilisés", *Revue de métallurgie*, **107**, p. 441-443 (2010).

15. R. Tricot, "Résistance à la corrosion des alliages de titane, de zirconium ou de tantale", Matériaux et Techniques, **7**, p. 297–307 (1987).

16. M. Pourbaix, *Atlas d'équilibres électrochimiques à 25°C*, Gauthier-Villars & Cie, Paris (1963).

17. J.-P. Schosger, "Contribution à la connaissance du comportement de l'acier Z3 CN 18-10 dans l'acide nitrique concentré, chaud et confiné", *Thèse de Doctorat de l'Institut National Polytechnique de Toulouse* (1996).

18. F. Balbaud et al., "Cathodic reactions involved in corrosion processes occurring in concentrated nitric acid at 100 degrees C", *European Journal of Inorganic Chemistry*, **2000**, *4*, p. 665-674 (2000).

19. D. Sicsic, F. Balbaud-Célérier, B. Tribollet, "Mechanism of Nitric Acid Reduction and Kinetic Modelling", *Eur. J. Inorg. Chem.*, **2014**, 6174–6184 (2014).

20. R. Lange et al., "On the kinetics of the nitrate reduction in concentrated nitric acid", *Electrochemistry Communications*, **29**, p. 25-28 (2013).

21. A.J. Bard and L.R. Faulkner, *Electrochemical methods: fondamentals and applications*, Second ed., John wiley & sons, inc (2001).

22. D. Briggs and M.P. Seah, *Practical surface analysis*, Vol.1, ed. J.W. Sons (1990).

23. M.P.D. Seah, "Quantitative Electron spectroscopy of Surfaces: A Standard Data Base for Electron Inelastic Mean Free Path in solids", *Surf. Interface Anal.*, **1**, *2* (1979).

24. B. Hirschorn et al., "Determination of effective capacitance and film thickness from constant-phase-

element parameters", *Electrochimica Acta*, **55**, *21*, p. 6218-6227 (2010).

25. M. Benoit, C. Bataillon, B. Gwinner, F. Miserque, C. Sanchez-Sanchez, B. Tribollet, V. Vivier, "Influence of a passive layer on the kinetics of an electron transfer reaction", *17th Topical Meeting of the International Society of Electrochemistry*, Saint-Malo, France (2015).

26. S.P. Tanuma, C.J. Powell, D.R. Penn, "Calculations Inelastic Mean Free Paths. 5 Data for 14 Organic Compounds over the 50-2000 eV Range", *Surf. Interface Anal.*, **21**, *165* (1994).

27. W.H. Gries, "A universal Predictive Equation for the Inelastic Mean Free Pathlengths of X-ray Photoelectrons and Auger Electrons", *Surf. Interface Anal.*, **24**, *38* (1996).

28. D.D. Macdonald, "The history of the Point Defect Model for the passive state: A brief review of film growth aspects", *Electrochimica Acta*, **56**, *4*, p. 1761-1772 (2011).

29. M.M. Lohrengel, "Thin Anodic Oxide Layers On Aluminum And Other Valve Metals - High-Field Regime", *Materials Science & Engineering R-Reports*, **11**, *6*, p. 243-294 (1993).

30. C. Vittoz, P. Fauvet, B. Fieulaine, "Zirconium corrosion in nitric acid containing traces of hydrofluoric acid", *Eurocorr 2011*, Stockholm (September 7th, 2011)

31. E.M. Vanderwall and E.M. Whitener, "Concentrated nitric and dilute hydrofluoric acid mixtures in dissolution of zirconium metal", *Industrial and Engineering Chemistry*, **51**, *1*, p. 51-54 (1959).

32. E.M.M. Sutter, F. Hlawka and A. Cornet, "Comparative behavior of titanium and zirconium in hydrofluoric nitric-acid pickling solutions", *Corrosion*, **46**, *7*, p. 537-544 (1990).

33. Z. Goncalves and H. Munzel, "Dissolution kinetiks of zircaloy in HNO_3/HF mixtures", *Journal of Nuclear Materials*, **170**, *3*, p. 261-269 (1990).

34. F. Hlawka and E.M.M. Sutter, "Reactivity of the surface of zirconium during pickling in nitrichydrofluoric acid", *Materials and Corrosion/Werkstoffe und Korrosion*, **42**, *8*, p. 428-436 (1991).

35. T. Smith and G.R. Hill, "A Reaction Rate Study of the Corrosion of Low-Hafnium Zirconium in Aqueous Hydrofluoric Acid Solutions", *Journal of The Electrochemical Society*, **105**, *3*, p. 117 (1958).

36. R.E. Meyer, "The electrochemistry of the dissolution of zirconium in aqueous solutions of hydrofluoric acid", *Journal of the Electrochemical Society*, **111**, *2*, p. 147-155 (1964).

37. J. Prono et al., "Dissolution-passivation model for zirconium alloys in fluorinated media", *In Proc. Int. Symp. environ. Degrad .mater. nucl. ANS.* (1992).

38. J. Prono, *Electrochimie du zirconium et de ses alliages en milieu nitrique fluoré*, Ecole Centrale Nantes: Nantes, p. 1-175 (1993).

39. J. Prono et al., "Anodic behavior of zirconium and its alloys in fluorinated nitric media dissolution-passivation model", *Journal of Applied Electrochemistry*, **25**, *11*, p. 1031- 1037 (1995).

40. B. Pihlar and Z. Cencič, "Investigation of a zirconium electrode as a sensor for fluoride ions", *Analytica Chimica Acta*, **273**, *1–2*, p. 267-274 (1993).

41. R.E. Meyer, "Rotating disk study of dissolution of zirconium in $HF-HNO_3$", *Journal of the Electrochemical Society*, **112**, *7*, p. 684 (1965).

42. J. Vehlow, "Corrosion of zircaloy-4 in H_2SO_4-NaF and its application for measuring the distribution pattern of fission-products in zircaloy-4 fuel hulls", *Werkstoffe Und Korrosion-Materials and Corrosion*, **36**, *5*, p. 195-202 (1985).

43. M.E. Straumanis, W.J. James, and W.C. Custead, "The difference effect and anodic behavior of zirconium dissolving in hydrofluoric acid", *Journal of the Electrochemical Society*, **107**, *6*, p. 502-506 (1960).

44. V.A. Gil'man and Y.M. Kolotyrkin, "The mechanism of the dissoluion of zirconium in acid solutions of fluorides", *Dokl. Phys. Chem.,* **155**, p. 384-387 (1964).

45. R.E. Meyer and S.M. Zettl, "Rotating disk study of dissolution of zirconium in $HF-H_2SO_4$", *Journal of the Electrochemical Society*, **112**, *11*, p. 1092 (1965).

46. S. Cattarin, M. Musiani, and B. Tribollet, "Nb electrodissolution in acid fluoride medium - Steady-state and impedance investigations", *Journal of the Electrochemical Society*, **149**, *10*, p. B457-B464 (2002).

47. W. Klas et al., "Bestimmung der Abtragungsraten von Zirconium, Tantal und der Legierung Tantal-40Niob in fluoridhaltiger azeotroper Salpetersäure mit Hilfe der Radiotracer-Methode", *Materials and Corrosion/Werkstoffe und Korrosion*, **42**, *11*, p. 570-575 (1991).

48. F.E. Heakal et al., "Effect of fluoride media on the stability of anodic ZrO_2 films", *Corrosion*, **46**, 3, p. 247-253 (1990).

49. G.A. El-Mahdy, S.S. Mahmoud and H.A. El-Dahan, "Effect of halide ions on the formation and dissolution behaviour of zirconium oxide", *Thin Solid Films*, **286**, *1-2*, p. 289-294 (1996).

50. N.S.D. Elayathu and J. Balachandra, "Studies on the passivation behaviour of some zirconium base alloys in nitric acid solution containing fluoride", *J. Electrochem Soc. INDIA*, p. 243 – 250 (1973).

51. H.G. Zimmermann, "Pickling of zirconium alloys", *Journal of Nuclear Materials*, **11**, *2*, p. 247-248 (1964).

52. D. Kowalski, D. Kim, and P. Schmuki, "TiO_2 nanotubes, nanochannels and mesosponge: Self-organized formation and applications", *Nano Today*, **8**, *3*, p. 235-264 (2013).

53. P. Roy, S. Berger and P. Schmuki, "TiO2 Nanotubes: Synthesis and Applications", *Angewandte Chemie-International Edition*, **50**, *13*, p. 2904-2939 (2011).

54. H.K. Chen and Z.F. Gong, "Oxidation behaviour of molten ZK60 and ME20 magnesium alloys with magnesium in 1,1,1,2-tetrafluoroethane/air atmospheres", *Transactions of Nonferrous Metals Society of China*, **22**, *12*, p. 2898-2905 (2012).

55. P. Cong, J. Imai, and S. Mori, "Effect of gas pressure on tribological properties and tribochemical reactions of alumina sliding against zirconia in HFC-134a", *Wear*, **249**, *1-2*, p. 143-149 (2001).

56. P. Cong and S. Mori, "Tribochemical effects on tribological properties of self-mated zirconia ceramic in HFC-134a gas", *Tribology Letters*, **17**, *2*, p. 261-267 (2004).

57. R.R. Hammer, *Determination of the stability constants of a number of metal fluoride complexes and their rates of formation*, p.1-111 (1979).